Future Scenario Earthquakes: Dynamic Rupture simulation on the Wenchuan-Maoxian Fault in the Longmen Shan, China, thrust belt

Rongjiang Tang[1,2], Ryosuke Ando[2]

[1] Yangtze Delta Region Institute of University of Electronic Science and Technology of China, Huzhou, Zhejiang, China

[2] Department of Earth and Planetary Science, School of Science, University of Tokyo, Bunkyō, Tokyo, Japan

Corresponding Author

Ryosuke Ando ando@eps.s.u-tokyo.ac.jp

Key points:

1. We develop a new method to refine fault geometry through inverting long-term slip rates, based on the Wallace–Bott hypothesis.

2. General rupture patterns for earthquake scenarios on Wenchuan-Maoxian Fault and Lixian fault are evaluated and could fall into three groups.

3. The rupture starting on the reverse oblique-slip tends to jump to the strike-slip fault, but the reverse process is suppressed.

Abstract: The 2008 Wenchuan Mw 7.9 mainshock has caused catastrophic destruction to cities along the northwestern margin of the Sichuan Basin. The Wenchuan-Maoxian Fault (WMF) on the hinterland side, along with a conjugate buried Lixian fault (LXF) was not activated by this earthquake but is likely to experience large earthquakes in the future. We perform 3D dynamic earthquake rupture simulations on the WMF and LXF to access the possibility of the earthquake occurrence and further explore the possible size of earthquakes and the distribution of high seismic risk in the future. We firstly invert focal mechanism solutions to get a heterogeneous tectonic stress field as the initial stress of simulation. Then we develop a new method to refine fault geometry through inverting long-term slip rates. Several fault nucleation points, friction coefficients, and initial stress states are tested, and the general rupture patterns for these earthquake scenarios are evaluated and could fall into three groups. Depending on initial conditions, the dynamic rupture may start in the LXF, leading to magnitude-7.0 earthquakes, or start in the WMF, then cascades through the LXF, leading to magnitude-7.5 earthquakes, or both start and arrest in the WMF, leading to around magnitude-6.5 or 7.0 earthquakes. We find that the rupture starting on the reverse oblique-slip tends to jump to the strike-slip fault, but the reverse process is suppressed. The rupture propagating eastward causes larger coseismic displacements than the westward propagation, and relatively high peak ground velocities are distributed near the northeastern end of WMF.

Plain Language Summary: The 2008 Wenchuan Mw 7.9 earthquake has caused catastrophic destruction to cities and counties along the northwestern margin of the Sichuan Basin. The Wenchuan-Maoxian Fault (WMF) on the hinterland side, along with a conjugate buried Lixian fault (LXF) did not slip in this event but is likely to experience large earthquakes in the future. We perform 3D dynamic earthquake rupture simulations on the WMF and LXF to access the possibility of the earthquake occurrence and further explore the possible size of earthquakes and the distribution of high seismic risk in the future. We infer the tectonic stress field from the focal mechanism solutions, to set up as the initial state of simulation. Then we develop a new method to refine fault geometry through inverting long-term slip rates. We simulate several earthquake scenarios, to quantify probable rupture pattern for future earthquakes in the target area, the fault system of the WMF and LXF. This process is to clarify the mechanical causality of the dynamic system. Numerical simulation results forecast the possible size of the earthquakes and the potential high seismic risk areas occurring on the WMF and LXF in the future while the timing is out of focus.

1 Introduction

The 2008 Mw7.9 Wenchuan earthquake caused devastating destruction to cities and counties along the active faults of the Longmen Shan thrust belt. Three parallel NW dipping fault zones, from hinterland to foreland being the Wenchuan-Maoxian fault, the Beichuan fault, and the Pengguan fault, constitute the crustal structure of the Longmen Shan fault zone (LMSFZ) (Figure 1), and the mainshock and aftershocks only rupture the BCF and PGF (Xu et al.,2009; Feng et al.,2017; Liu-Zeng et al., 2009). Several counties including Yingxiu, Beichuan, Nanba have suffered a devasting disaster in this event, one of the obvious reasons is that the fault almost passes through the center of the counties (Figure 1). Similarly, the WMF also passes through the urban areas of Wenchuan, Maoxian and several towns, and more than 200

thousand inhabitants live in the area along this fault. Should an earthquake in the future occur on the WMF, it would cause significant hazards to densely populated towns.

Yingxiu and Beichuan towns suffered the most intensive shock in the Wenchuan earthquake, which has been confirmed by previous inversion works and dynamic models (Hao et al., 2009; Shen et al., 2009; Zhang et al., 2011; Tang et al.,2021a). If numerical simulations can be used in advance to predict the rupture characteristics of future earthquakes, especially the position of maximum slip patches, can the huge mortality of 2008 Wenchuan earthquake be significantly reduced? If the WMF has the potential to produce a strong earthquake in the future, how large the earthquakes on the WMF may occur? Dynamic rupture simulations can intrinsically simulate physically self-consistent features of earthquake behavior, being able to simulate an unknown earthquake given under given stress conditions and fault geometry. This makes it a natural choice to investigate a future scenario earthquake on the WMF.

In contrast to the approach that we present in this paper, most of previous dynamic simulations have been used to investigate large earthquakes that had already occurred, with abundant prior information being available to constrain fault geometry and regional stress field (Zhang et al.,2019; Ando et al.,2017; Ulrich et al.,2019; Tang et al.,2021a). For instance, early aftershock locations can also help constrain the geometry of seismogenic fault that ruptured during the mainshock (Yin et al.,2018; Wu et al.,2017; Wang et al.,2021), so do the earthquake focal mechanism solutions (FMS) containing information of characteristics of the fault geometry. Many researchers use the FMSs from foreshocks or aftershocks to invert the regional stress, which can be resolved onto the fault surface as initial condition of dynamic earthquake simulation (Zhang et al.,2019; Ando et al.,2017; Ulrich et al.,2019). However, simulating an unknown and reliable earthquake in the future, such as this work, is a challenge due to the lack of sufficient seismological evidence to build a dynamic model.

Fortunately, the WMF is close to the Wenchuan main shock: BCF, and there are still some aftershocks distributed along the WMF. Together with the fact that the tectonic stress field usually changes slowly in a small range, it enables us to use the focal mechanism solutions of aftershocks to invert the regional stress field near the WMF. Nevertheless, the aftershocks along the WMF are very limited, especially in the northern portion, which is not enough to provide accurate constrain for geometry of numerical simulation (Wu et al.,2009; Zhao et al.,2010; Yin et al.,2018). To solve this problem, we propose a new optimal method to obtain the fault geometry of WMF by inverting the long-term slip rate, based on the Wallace-Bott hypothesis (Wallace 1951; Bott, 1959), which asserts that rigid blocks slide linearly with respect to each other along a planar fault in the direction of the maximum resolved shear stress. The goal of this algorithm is to find optimal geometrical parameters by the conjugate gradient method, to minimize the difference of directions between long-term slip rate and tangential traction, supposing that regional stress has been determined and resolved to the fault surface. In this case, we can constrain the geometry of any fault using the measured long-term slip rate, regardless of whether earthquakes have been recorded before.

It is worth pointing out that relocation of the Wenchuan earthquake sequence revealed an NW-SE-striking buried Lixian fault (LXF, shown in Figure 1) with a length of ~50 km, roughly perpendicular to the WMF with oblique dextral slip sense. Considerable pure strike-slip type aftershocks (Cai et al.,2011; Yi et al.,2012; Li et al.,2019; Yang et al.,2021) along the LXF reveal an almost vertical fault plane and sinistral strike-slip. The cross-cutting geometry and opposite slip senses of these conjugate faults raise questions

about fault interactions. Whether the ruptures starting from different nucleation positions cascade through another fault to form a greater disaster than a single earthquake, or get arrested near the fault intersection?

In this study, we first calculate the distribution of heterogeneous stress fields near the WMF based on the focal mechanism solutions (FMS) of earthquakes ($M \geq 3.5$). In contrast to the previous studies involving tectonic stress analysis of LMSFZ (Li et al.,2019), we focus on obtaining reliable heterogeneous stress tensor distribution including isotropic and deviatoric parts, such that we directly apply the inverted stress to the numerical simulation, without any trial-and-error approach (Douilly et al., 2015; Ulrich et al.,2019; Xu et al.,2019; Lozos and Harris, 2020) to obtain a stress condition fitted to aimed coseismic slip distributions. Then, we apply the conjugate gradient algorithm to invert long-term slip rate to get the optimal geometrical parameters. Subsequently, we implement the several dynamic rupture computational simulations to investigate physics-based scenarios of large earthquakes on the WMF and LXF, aim at exploring how big an earthquake may occur on these two faults in the future, and evaluate the possible distribution of high seismic risk.

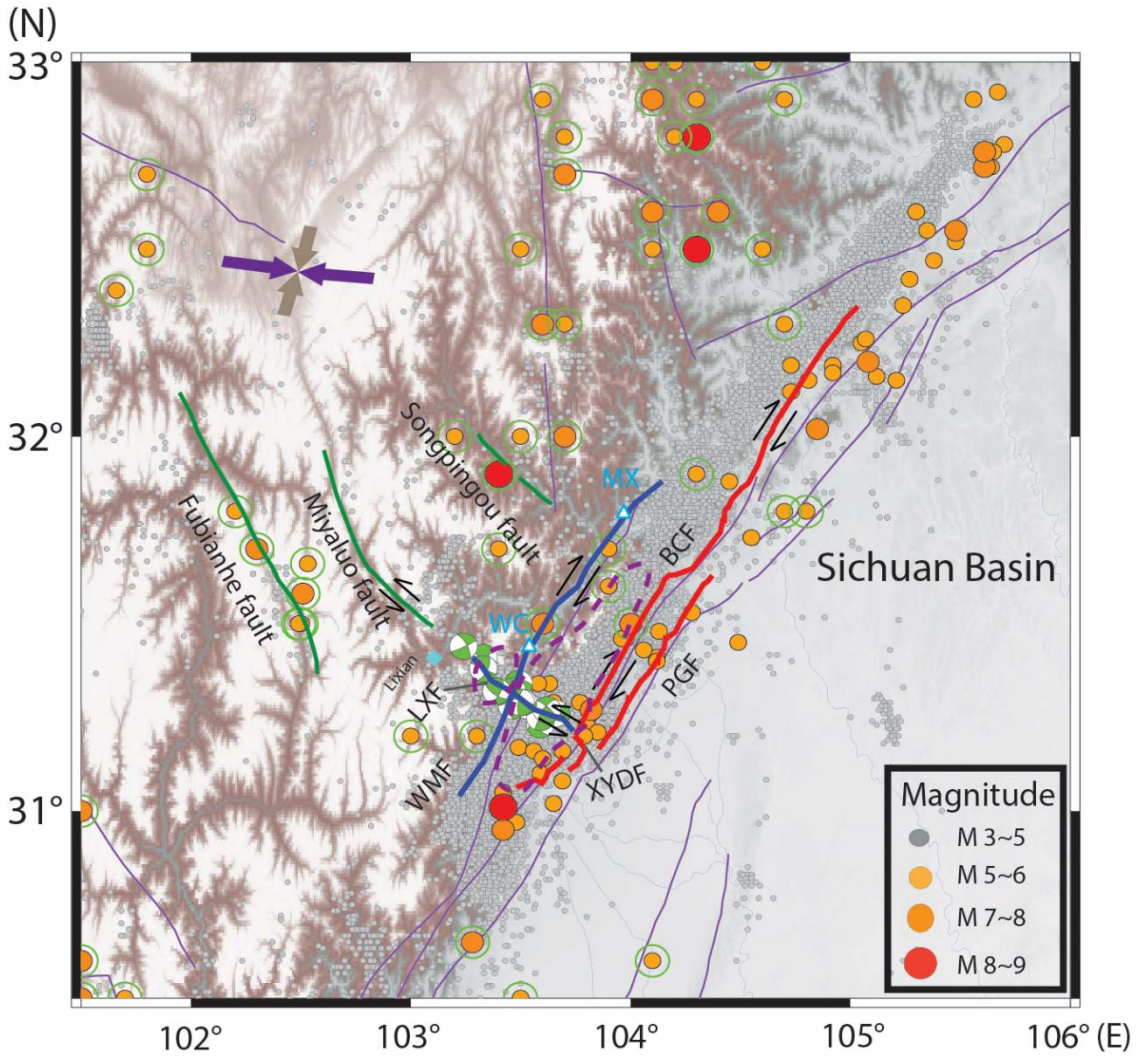

Figure 1 Map showing the setting of major faults of the center Longmen Shan fault zone. The red bold black lines indicate the field-confirmed rupture traces in Wenchuan earthquake (Xu et al.,2009; Liu-Zeng et al.,2009). The blue solid lines represent the WMF and Lixian faults, both of which did not slip in the mainshock but are very active in aftershocks. The green solid lines represent three active faults parallel to the LXF. Accurate fault trace of the WMF is derived from field investigation of Xie et al (2011), and the location of the LXF trace is deduced from the distribution of pure strike-slip aftershocks (Li et al.,2019). Historical earthquake catalog denoted by filled circles refers to Wang et al (2021) and China Earthquake Networks Center (http://data.earthquake.cn). Green hollow circles denote the historic strong earthquakes (M>5) before 2008 Wenchuan event. The purple and gray coupled arrows depict the maximum, and minimum horizontal compressional stress fields (Luna and Hetland, 2013). The third primary stress (not shown) is vertical. The purple dashed circles respectively show the positions of Xuelongbao (north) and Pengguan (south) Massif (Shen et al, 2019). WC-Wenchuan. MX-Maoxian.

2 Seismicity and potential seismic risk in the Wenchuan-Maoxian fault and Lixian Fault

Firstly, the WMF has prominent similarities in fault orientation and geometry to the BCF and PGF caused the 2008 mainshock. The three faults are spatially subparallel and horizontally spaced within 20km (Figure 1). Also, they may root into the same main detachment with a depth of around 20 km and the main fault shapes display an essentially classic ramp-flat geometry (Hubbard et al 2010; Jia et al.,2010; Li et al.,2010). The simulation of Tang et al. (2021a) reveals that Wenchuan mainshock has changed the stress status on the WMF, forming a positive Coulomb failure stress change in the center portion of the WMF, suggesting that the 2008 mainshock may clock-advance the earthquake cycle of the WMF, though to a limited extent (the fault perpendicular extent of the stress change is limited by the seismogenic depths, comparable to the fault separation of 20 km). The WMF on the hinterland side was not activated by the 2008 event, but we presume that this fault has potential to experience an earthquake in the future, while the timing cannot be specified.

Second, field investigations and exhumation studies of the central Longmen Shan show that the WMF has mainly exhibited dextral strike slip faulting with the comparable reverse component (Tang et al.,1991; Zhou, et al.,2007; Shen et al,2019; Tian et al., 2013; Tan, Xu, et al., 2017) since the Late Cenozoic, which is consistent with the coseismic slip sense as well as the long-term slip rate of BCF and PGF (Zhou et al.,2007; Densmore et al., 2007; Xu et al.,2009; Liu-Zeng et al., 2009; Feng et al.,2017). Shen et al (2019) collected samples from the two vertical transects from the central and southern sides of the Xuelongbao massif, to extract apatite and zircon for fission track and (U-Th)/He analysis. The exhumation history of the Wenchuan-Maoxian fault can be constrained to around 0.6 mm/yr of long-term slip-rate, which is similar to that along the frontal BCF (~0.54 mm/yr before Wenchuan earthquake (Zhou et al.,2007) and 0.88~0.91 mm/yr after Wenchuan event (Ran et al.,2013)), suggesting that the WMF may have the comparable intensity of tectonic activity as the BCF to accommodate significant crustal deformation over the long-term, even though it was not ruptured by the 2008 Wenchuan earthquake.

In addition, the modern earthquake catalog provides evidence that three major faults have comparable seismic activities. According to observational records before Wenchuan earthquake (Figure S1), three strong earthquakes (6<M<6.5) have occurred in the middle Longmen Shan: April 1657 M6.5 in Wenchuan, February 1950 M6.2 in Beichuan and February 1970 M6.2 in Dayi. A total of 11 moderate

earthquakes (5<M<6) in this area were distributed over three faults, with 4 earthquakes occurring near the WMF, according to Data Sharing Infrastructure of National Earthquake Data Center (http://data.earthquake.cn) (see Figure S1). Due to the low historical seismicity and limited (<3 mm/yr) geodetic observations (Chen et al.,2000), it was not until the occurrence of Ms8.0 Wenchuan earthquake in 2008 that high seismic risk in the central Longmen Shan was generally realized by most researchers. It is important to note, a total of 12 $Ms > 5.6$ aftershocks occurred within one year after the Wenchuan earthquake, of which three occurred in the WMF and one in the LXF.

The buried Lixian fault may be active, located as bridging the WMF and the BCF, although insufficient evidence has been collected on the surface. Geological survey is very scant for this fault due to the heavy vegetation cover and rugged terrain, and the maximum elevation difference exceeds 3 kilometers (Tan et al., 2017). Further to the northwest along the aftershock belt, the Miyaluo fault is exposed (Figure 1). It displays a sinistral sense of slip with unknown slip rates and has been active during the Pleistocene (Yang and Zhang, 2010; Wang et al., 2015). Yang and Zhang (2010) have dated twelve samples of metasediments and granites taken from the Miyaluo Fault, WMF and BCF using apatite fission track dating (FT) method. These samples were collected in the developed fracture zone of rock mass, with FT ages significantly younger than the surrounding rocks, indicating the most recent tectonic activities. The results show that the high activity of WMF and BCF occurred in the early Pleistocene (FT ages of 1. 2 ～ 1. 3 Ma); the Miyaluo fault developed in the interior of the plateau was also highly active in the middle Pleistocene (around 0. 5 Ma). Despite the lack of direct geological evidence, we suspect that the Miyaluo fault may still have been active in the Holocene, since several destructive earthquakes (larger than M7) were recorded on the two sub-parallel faults: the Fubianhe and Songpinggou faults with NW strike orientation, conjugating the BCF (Figure 1). After the Wenchuan event, it is also possible that the fracture along the LXF propagates toward the Miyaluo fault in the future. In the following chapter of stress inversion analysis, we will find that the LXF exhibits the most favorable orientation in the regional stress field. Therefore, LXF may display a relatively high seismic risk, although none of the great earthquakes has been recorded recently.

The 2008 Wenchuan main shock and aftershocks released a large amount of stress or elastic energy along the BCF and PGF, resulting in a low seismic risk for a long period in the future. On the contrary, the WMF has not experienced a strong earthquake for more than 360 years since the possible last M6.5 earthquake in 1657, and the current earthquake interval completely excess a moderate earthquake (5<M<6) cycle (Figure S1). In addition, positive Coulomb failure stress change from 2008 mainshock may increase seismic activities in the regions with loaded stress on WMF. Consequently, incorporating abovementioned factors, we suggest that the WMF may have the potential to produce a strong earthquake with M>6.5 even M7 in the future, while the timing is out of focus.

3 Regional stress inversion and modeling

The initial stress plays a fundamental role in controlling dynamic rupture processes. We infer the present regional tectonic stress field by inverting earthquake focal mechanism solutions (from Li et al., 2019) of aftershocks of 2008 Wenchuan earthquake as a reference to the future earthquake scenario in this region. We adopt a damped linear stress inversion method developed by Hardebeck and Michael (2006) to

determine the stress field using FMSs. This method enables us to infer the directions of the principal stresses σ_r (r = 1, 2, 3 for the maximum, intermediate and minimum principal stresses, respectively) and a ratio between the principal stresses σr, defned as $\emptyset = (\sigma_2 - \sigma_3)/(\sigma_1 - \sigma_2)$. The details of the method and results are described in the supplementary Text S1.

However, to be inputted into our dynamic rupture simulation, these observationally constrained parameters are insufficient to determine the absolute values of the principal stresses. Two unknowns are needed by imposing other prior information. For simplification, we firstly assume that one of the principal stress axes is in the vertical based on the observation near the WMF as expected from Anderson (1951). Then we constrain one unknown as the $\sigma_H/\sigma_v = 1.6$, given an approximate value from the In-situ stress measurements along the Beichuan-Yingxiu fault after the Wenchuan earthquake (Qin et al.,2013), where σ_H and σ_v denote the magnitudes of the maximum horizontal principal stress and the vertical principal stress. The σ_H along the depth is constrained by assuming the average stress drop satisfies the stress drop derived from empirical relations (Kanamori and Anderson, 1975). We assume typical overburden stress and the pore pressure increase with the depth, and the latter gradient gradually approaches the former (Rice, 1992), such that the stresses is tapered to the ambient value at a certain depth (here we set 5 km) (Rice, 1993). The resulting stress field model is shown in Figure 2 as plotted on the surface of WMF. The along-strike rotation of the principal horizontal stresses reflects our inversion result.

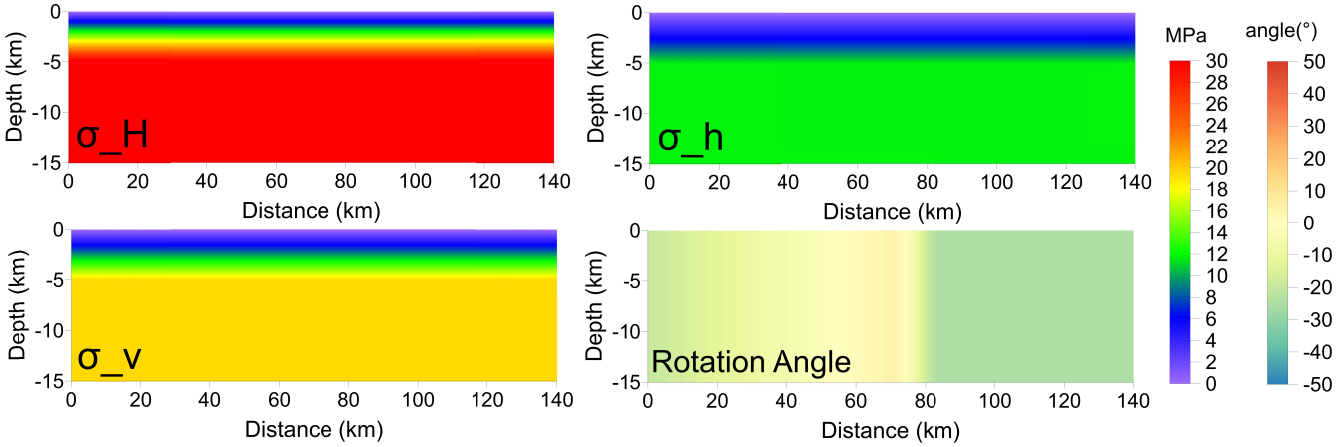

Figure 2 Along strike distribution of three-component principal stress (σ_H, σ_h for the maximum and minimum horizontal principal stresses, σ_z for vertical principal stresses). The lower right Figure shows the angle between the east and the maximum horizontal stress axis (Negative denotes the clockwise).

4 Fault Geometry modeling and new inversion method

Our dynamic model is built to reproduce the observed oblique dextral-slip WMF and almost pure sinistral strike-slip LXF (Figure 1). We set the LXF as vertical, with 0.5 km buried depth, as well as 15 km basal depth inferred from average seismogenic depth (Shen et al., 2009; Wan et al.,2017; Ramirez-Guzman and Hartzell, 2020). In the simulation we assume an artificial boundary on the northern end of the LXF, not to extend northward and link the Miyaluo fault (Figure 1). Many studies over the last decade focused on the

geometry of the BCF and PGF through detailed relocation of aftershocks (Wu et al.,2009; Zhao et al.,2010; Yin et al.,2018) and seismic reflection data (Hubbard et al., 2010; Jia et al., 2010; Lu et al.,2014), as well as joint inversion of GPS and InSAR measurements (Shen et al.,2009; Wan et al., 2017). Yet the geometry of WMF fault is still unclear so far, due to the scant investigations of seismic reflection, and its aftershocks are very limited, especially in the northern portion.

Here we develop a new method to refine the fault geometry of WMF by inverting the long-term slip rate, based on the abovementioned regional stress field and the Wallace-Bott hypothesis (Wallace 1951; Bott, 1959). The basic assumption of the current method is that the slip direction (the rake angle) is parallel to the maximum shear traction on the fault, determined by the inferred principal stresses and the orientation of the fault plane. A model of listric fault geometry is considered, which is allowed to vary continuously along strike to utilize the data of the surface fault traces. The downdip fault geometry follows the form (Wan et al.,2017):

$$z(y) = \frac{2h_0}{\pi}\arctan(y/\tau), \quad (1)$$

where z is the depth of the fault plane, and y is the horizontal distance of the fault plane from its surface trace. The fault surface is described by the B-spline allowed to vary continuously along strike, with its downdip curvature dictated by the parameter τ. h_0 is the fault depth to be solved for, and assumed to be the same for all the fault segments. In this nonlinear inversion, the model parameters include a total of the 10 downdip curvature parameter τ uniformly distributed along the fault strike (around 16 km spatial interval), plus h_0 for all curves. Under the condition that the values of τ can accurately describe the surface trace and the non-planar fault surface, we expect as few parameters as possible to avoid the over-fitting problem due to limited observed data. We collected both the vertical and horizontal components of the long-term slip rate from a few studies (Ma et al.,2005; Zhou et al.,2007; Ran et al.,2013; Shen et al., 2019) shown in Figure 3, and a total of 5 measured points with 7 slip-rates along the WMF are implemented in the inversion. Although the distribution of collocation points does not well cover the whole fault area, this analysis is useful to constrain the first-order feature of WMF geometry. The details of our geometry inversion method are further elaborated in the supplementary Text S2.

Long-term slip rate can't be accurately measured due to the uncertainty of geological age estimation of sediments (Zhou et al.,2007; Shen et al., 2019). To get a more reliable result, the inversion uncertainty is estimated using 100 bootstrap resamplings of the entire data set (7 slip-rates), and data from each measured point obey a Gaussian distribution. For each inversion, we set the same initial model with τ=5, $h_0 = 18\ km$ (Figure 4a). In addition, a few aftershocks are distributed at the south end of WMF (Figure S2), which is useful as prior information to constrain one of the inversion parameters. We can well fit the distribution of aftershocks using equation (1) with τ=3.5, $h_0 = 18\ km$. Therefore, the parameter τ at the southernmost position ($x = 0\ km$) is a force to keep little variation during the inversion.

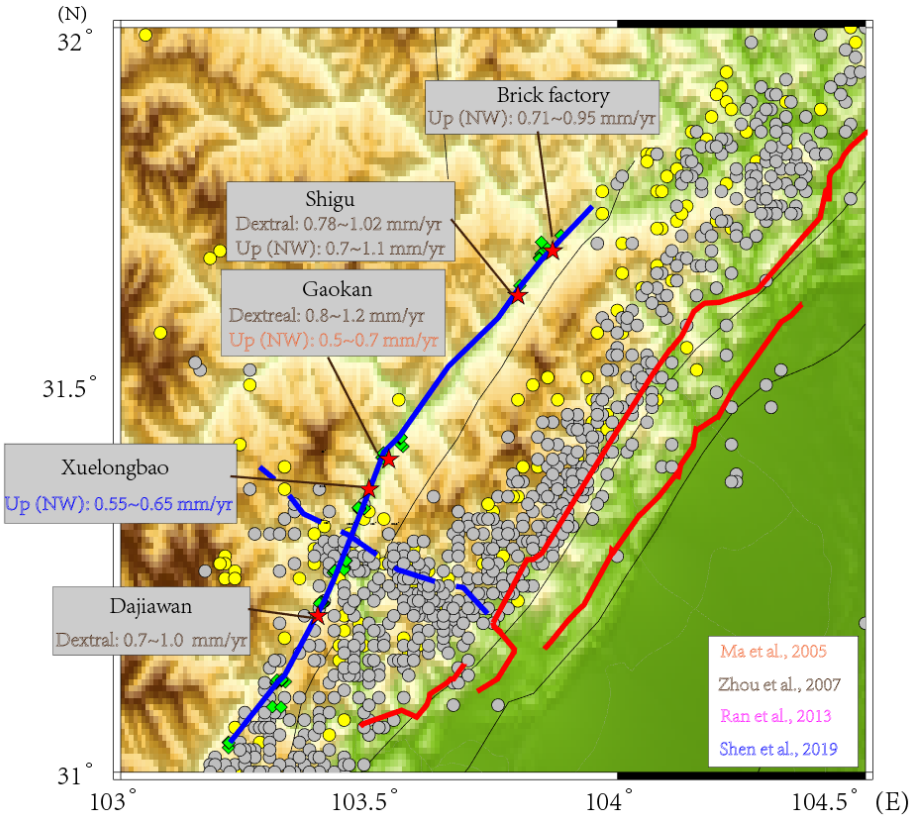

Figure 3 Map showing the measured points of long-term slip rate along the WMF. Each gray box contains the locations and long-term slip rates measured from different researchers. Dextral means dextral strike-slip rates and Up (NW) vertical slip rates with northwestern block being hanging wall. The red and blue lines are the same with Figure 1. Accurate fault trace of the WMF is from field investigation (green diamonds) of Xie et al (2011), and red stars denote the measured point positions of long-term slip rate. Gray circles present aftershocks of the 2008 earthquake (Yin et al.,2018).

The average of 100 inversions is derived to obtain the final fault model (Figure 4b), where dip angles near the surface varied along the fault strike due to the constraint of observed long-term slip rates (Figure 4c). The final inversion results are distributed in a narrow strand (Figure 4d), and all objective functions steadily decrease versus the iterations (Figure 4e), which justifies our method.

While we believe that the present method of fault geometry inversion is a powerful and physically-based tool when we do not have sufficient subsurface data, this method should involve ambiguities due to the limitations of the available data and model constraints. Actual fault geometry can have a larger variation; Wan et al. (2017) inferred the fault dip for the Wenchuan earthquake using composite geodetic data and found that the BCF dips at 36° near the surface at its southwest end and is close to vertical (83°) at its northeast end at the surface. Differences in the dip angle can lead to differences in rupture scenarios and seismic risks for the BCF and WMF. A more detailed analysis will be conducted in our future study.

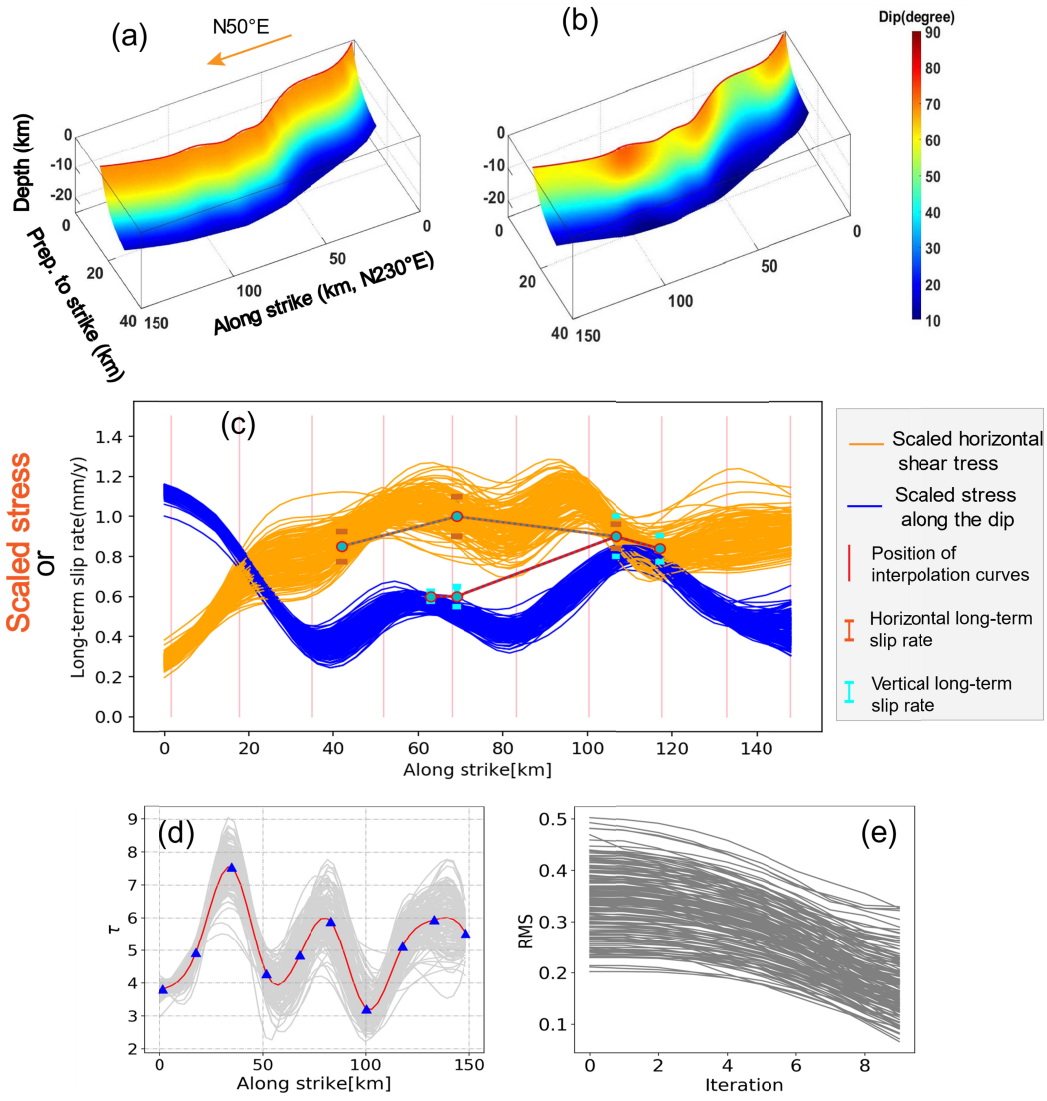

Figure 4 Estimation of fault geometry using 100 inversions. (a) Initial fault surface derived from the initial value of τ=5.0, $h_0 = 18$. (b) Final fault surface derived from average τ of 100 inversions; The average of inverted fault depth $h_0 = 16.11$ is not shown here. (c) Observed long-term slip rates and scaled traction. The blue and orange lines present weighted average shear stress along the dip and strike, respectively. The length of the bar indicates the standard deviation of slip rate. The vertical thin pink lines indicate the position of interpolation curves. (d) Distribution of inverted parameters τ, the red line is the average of 100 inversions (gray lines), and blue triangles indicate the position of interpolation curves. (e) Objective functions versus iterations from 100 inversions.

5. Dynamic rupture simulation

5.1. Method

We computationally simulate spontaneous dynamic rupture propagation on the conjugate fault system of WMF and LXF. The dynamic rupture problems are numerically solved by the Fast Domain Partitioning Boundary Integral Equation Method (Ando, 2016; Ando et al., 2017; Ando et al., 2018), which increases the efficiency of the elastodynamic boundary equation method (BIEM) without degradation in accuracy. We consider a homogeneous elastic half space, with Lamé parameters $\lambda = \mu = 28\ GPa$, and mass density $\rho = 2776\ kg/m^3$ ($v_p = 5500\ m/s, v_s = 3175\ m/s$). These parameters are based on the first-order approximation of a three-dimensional velocity structure around the Longmen Shan fault obtained from seismic tomography (Pei et al.,2010; Wang et al.,2021). Note that the local variation of shallow seismic velocity structures or the site effect amplifying ground motion is not included in the present model. Rather, we focus on the source effect.

The boundary condition for the fault surface is considered where frictional strength is described by the linear slip weakening friction law

$$T_s = \left(\mu_d + (\mu_s - \mu_d)\frac{S}{D_c}\right) T_n\, H(D_c - S) \tag{2}$$

Where D_c, μ_s and μ_d denote the characteristic slip, and the static and dynamic frictional coefficients, respectively. T_s and T_n denote the shear traction and normal stress. Based on the results of high-speed friction experiments (Yao et al, 2013), we set friction coefficients uniform on the entire fault with $\mu_s = 0.53$， $\mu_d = 0.12$. We choose $D_c = 0.8\ m$ because its upper bound is estimated in the range of 1.0~2.0 m by Tang et al (2021a), who applied the approach proposed by Mikumo et al. (2003) to estimate the upper bound of Dc of 2008 Wenchuan earthquake, constrained by the slip rates on the fault points from the kinematic inversion (Zhang et al.,2014) of complete near-field waveforms. The neighboring parameter space is also investigated and discussed in section 6, considering the uncertainties of these parameters. It is important to note that we first chose the relatively low μ_s, μ_d and Dc to allow the rupture to propagate to artificially assumed boundaries without being arrested, such that the worst earthquake scenarios can be explored.

In the simulation, ruptures are triggered by overstressing a small circle patch with a radius 3 km, where the initial stress is uniform and slightly above yield stress. Once a rupture is triggered, its subsequent development is controlled by the elastodynamic equation, frictional law, initial stress as well as fault geometry. While long-term slip rate and seismicity on the WMF indicate the potential to produce a large earthquake in the future, under our current state of knowledge, it is difficult to predict a probable hypocenter. Therefore, we considered five different nucleation locations, respectively located at the center, east and west ends of the WMF, and the north and south end of the LXF.

5.2 Results

5.2.1 Coseismic slip

Figure 5 shows the total slip distribution of the WMF and LXF, as well as the moment magnitude in each case. We find that the rupture tends to jump from the oblique-slip fault (WMF) to the strike-slip fault (LXF), but the reverse is more difficult. For instance, a dynamic rupture may start in the central, eastern or western parts of WMF, then cascade to the LXF, leading to three comparable-sized earthquakes with magnitude-7.56 ,7.55 or 7.57. However, if it starts in the south or north of LXF, triggering a second

rupture on the WMF will be difficult (Figure 5, video S1-S2), leading to a smaller earthquake with a moment magnitude 7.05 or 7.06.

The total slip on the LXF is smaller than that of the WMF. This might be surprising because the stress drop on the LXF is significantly larger than that on the WMF (Figure S3). Noting that friction coefficients on the two faults are exactly the same, so the prominent difference of the coseismic slips should be caused by the faulting type and geometry. The WMF is a thrust fault with a larger extent in dip and strike than LXF, which is a buried and smaller purely strike-slip fault. In the same stress condition, larger faults tend to slip more due to the length-slip scaling. The free surface effect is further reduced for buried faults. Besides, thrust faults have been proved by numerical simulations to have larger coseismic slips than normal and strike-slip faults (Oglesby et al., 2002; Tang et al., 2021b), because the reflected waves from the free surface amplify the motions of the reverse fault near the free surface. This result indicates reverse faults may have greater destructive potential than strike-slip fault even though it is in a lower stress condition.

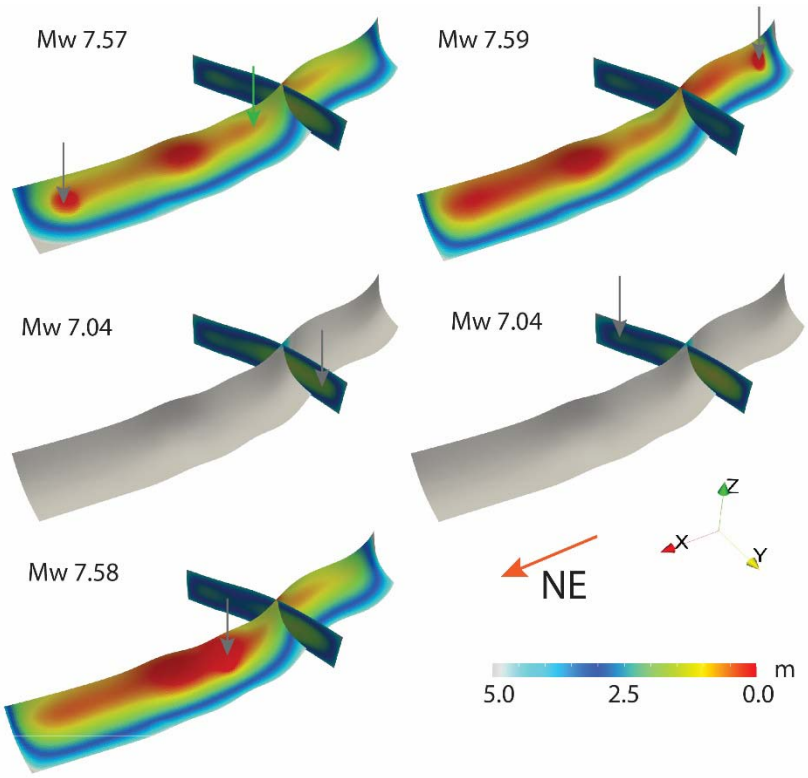

Figure 5 Total slips and earthquake magnitudes from different nucleation points noted by grey arrows. The green arrow denotes the point in Figure 13.

5.2.2 Peak Ground Displacement and Velocity

We evaluate the seismic risk potential, in a relative manner, by comparing derived surface displacements (Figure 6) and peak ground velocities (PGV) (Figure 7). We find rupture directivity effects caused by different nucleation positions lead to a prominent spatial difference in surface displacements and PGV. The site where the rupture front propagates toward will surfer stronger ground motions than the site where

the rupture propagates away due to the cumulative effect of the seismic radiation called the forward directivity (Somerville et al.,1997).

The ground motions of the hanging wall in the center and the eastern portion of WMF are significantly enhanced if a rupture nucleates in the west and propagates to the eastern, compared to the cases when a rupture starts in the west or center of the WMF (Figure 6 and Figure 7). These differences may be related to the relationship between the hanging wall's horizontal movement and the rupture directivity, depending on the different contributions of the horizontal slip component, because the components y and z are almost the same for each case (Figure 6). We should care about a high seismic risk of the northeastern end of the WMF in two cases (Figure 7 b, c) because the PGV is relatively high when a rupture nucleates at the center or southwestern end of WMF, and the surface displacements are also high. From Figure 7 we can further deduce that if the earthquake starts in most of the area on the WMF, the southwestern and northeastern end of WMF may inevitably experience stronger ground motions.

Compared to the WMF, the PGV and surface displacements near the buried LXF are relatively low because rupture does not break the surface (Figure 7 d, e). In addition, the rupture directivity shows symmetry on strike-slip faults, and PGV shows a similar distribution when rupture starts from either north or south of the LXF. However, for the WMF as an oblique-slip fault, the ground motion will be enhanced if the rupture propagating direction is consistent with the movement direction of the hanging wall.

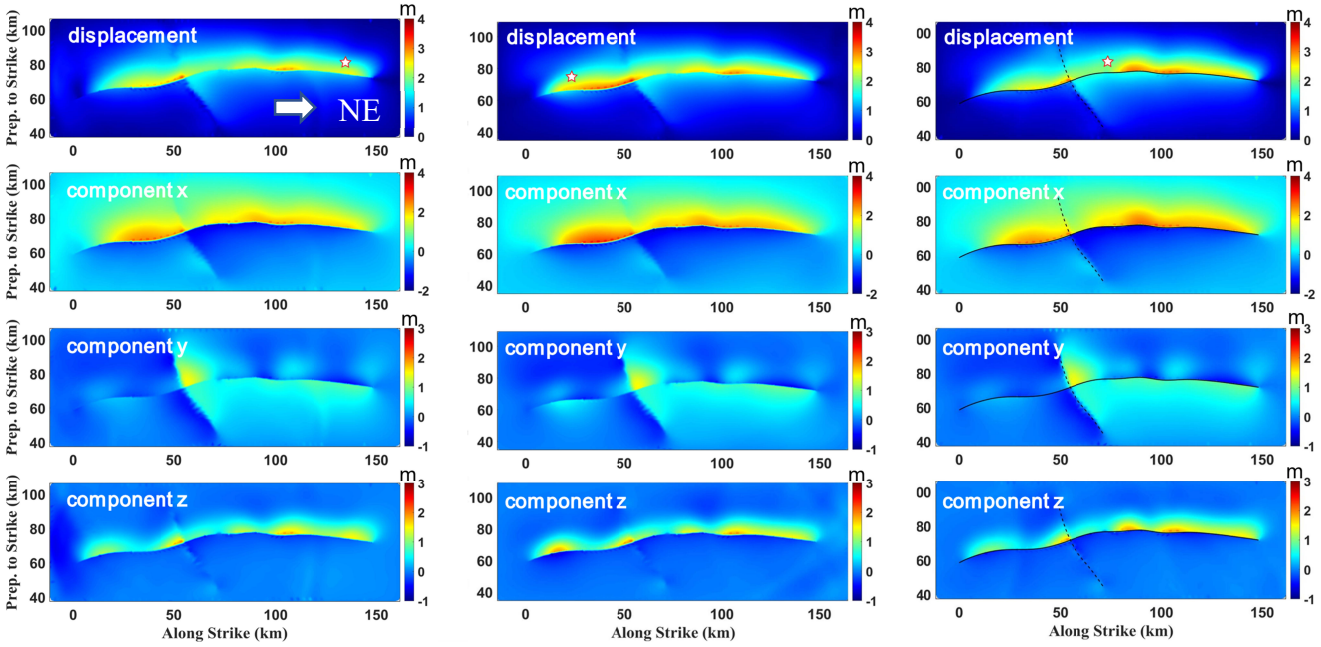

Figure 6 Three components and magnitude of surface slip, with eastern and western nucleation points. The white Pentagrams denote the epicenter. The white arrow indicates the NE direction. See Figure 5 for the definition of the x-y-z components.

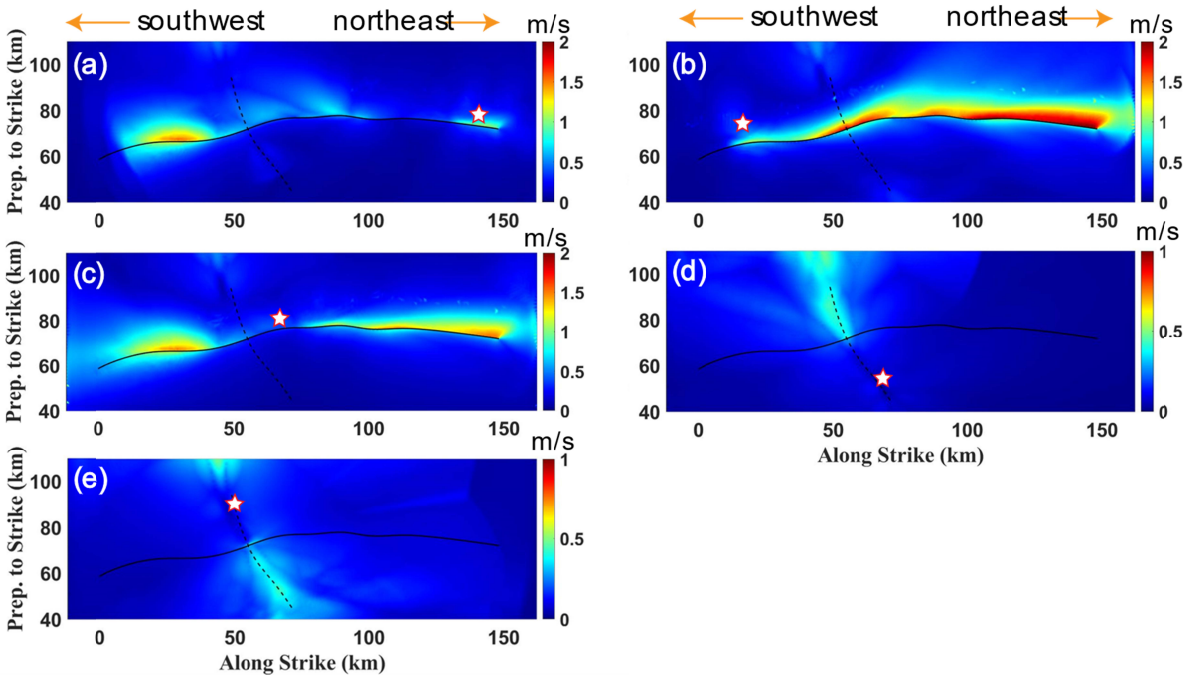

Figure 7 Magnitude of peak ground velocities from different nucleation points. The white pentagrams denote the epicenter.

6 Discussion

The worst-case scenarios have already been explored to evaluate the possible sizes of earthquakes and the distribution of strong ground motions. However, the results of dynamic rupture propagation are dependent on several key factors, including the initial stress, fault geometry, frictional parameters as well as hypocenters, which may lead to large uncertainty for different earthquake scenarios. For instance, different cases with a linear increase in stress from the surface down to some specified critical depth may result in a different distribution of ground motions as well as supershear transitions (Hu et al.,2021). To include this uncertainty, we change the specified depth but lower the maximum stress such that the same average stress drop can be held for the two cases (Figure 8). Without loss of generality, we model a total of 20 scenarios of dynamic rupture propagations (Table 1), to investigate the effects of neighboring parameter space, including μ_d (0.12~0.15) (Yao et al, 2013), Dc (0.8~1.2 m) (Tang et al.,2021a) and the critical depth of the stress increase.

Table 1

Models with a different set of friction and nucleation positions considered in this study.

Model	μ_d	D_c (m)	H of σ_v* (km)	*Depth of nucleation* (km)	M_w	Arrest*	Dynamic triggering*	Total Seismic Moment (N m)
E1	0.12	0.8	5	6.5	7.57	No	Yes	2.893×10^{20}
W1	0.12	0.8	5	6.5	7.59	No	Yes	3.070×10^{20}
S1	0.12	0.8	5	6.5	7.04	No	No	4.686×10^{19}

N1	0.12	0.8	5	6.5	7.04	No	No	4.704×10^{19}
C1	0.12	0.8	5	6.5	7.58	No	No	3.048×10^{20}
E2	0.12	0.8	5	9.5	7.56	No	Yes	2.825×10^{20}
W2	0.12	0.8	5	9.5	7.59	No	Yes	3.060×10^{20}
E3	0.12	0.8	10	6.5	7.00	Yes	No	4.080×10^{19}
W3	0.12	0.8	10	6.5	7.56	No	Yes	2.823×10^{20}
N3	0.12	0.8	10	6.5	7.05	No	No	4.796×10^{19}
S3	0.12	0.8	10	6.5	7.05	No	No	4.774×10^{19}
C3	0.12	1.0	10	6.5	6.93	Yes	No	3.129×10^{19}
E4	0.15	0.8	5	6.5	6.92	Yes	No	3.118×10^{19}
W4	0.15	0.8	5	6.5	7.5	Yes	Yes	2.225×10^{20}
C4	0.15	0.8	5	6.5	7.42	Yes	Yes	1.703×10^{20}
W5	0.15	1.2	5	6.5	6.62	Yes	No	1.088×10^{19}
N5	0.15	1.2	5	6.5	7.00	No	No	4.109×10^{19}
S5	0.15	1.2	5	6.5	7.00	No	No	4.106×10^{19}
E5	0.15	1.2	5	6.5	6.65	Yes	No	1.207×10^{19}
C5	0.15	1.0	5	6.5	7.38	Yes	Yes	1.509×10^{20}

H of σ_v*: the critical depth of the two different depth-dependent stress cases shown in Figure 9.
Arrest*: if Yes, the rupture will be arrested rather than reaching the assumed artificial barrier.
Dynamic triggering*: if Yes, the rupture on one fault will trigger the secondary rupture on the other fault.
The first letter of the model name represents the nucleation location, and E1~C1 have been elaborated in the result section.

6.1 Effect of critical depth of stress

The average stress drops on the WMF and LXF are roughly obtained from observations from 2008 Wenchuan earthquake, but how is the distribution of stresses along the depth is poorly constrained. The magnitude of principal vertical stress depends on the overburden pressure (density and depth), which may also be compensated with the increased pore pressure (Hardebeck & Okada, 2018). Thus, we build two depth-dependent shear and normal stress regimes with the same average stress drop $\Delta\sigma_w = 2.9MPa$. The result of the first case has already been discussed in the result section, while the second case leads to the prominent different earthquake scenarios and distributions of the coseismic slip (Figure 8). For the second case with deeper critical depths, the ruptures starting in the east or center of the WMF propagate to 20 km beyond the nucleation area and arrest at the patch where the normal stress is stronger (Figure S3). In addition, the rupture from the west part propagates over the WMF and cascades to the LXF, but leads to lower magnitude (Table 1) and coseismic slips than that of W1 (Figure 5). However, contrary to the scenarios on the oblique fault (WMF), the coseismic slip and magnitudes on the sinistral fault (LXF) are slightly larger than that of case 1. These phenomena suggest that depth-dependent stress patterns may affect dip-slip faults more than strike-slip faults, and a larger stress gradient near the free surface of an oblique-slip fault is more likely to trigger stronger coseismic slip and higher seismic risk.

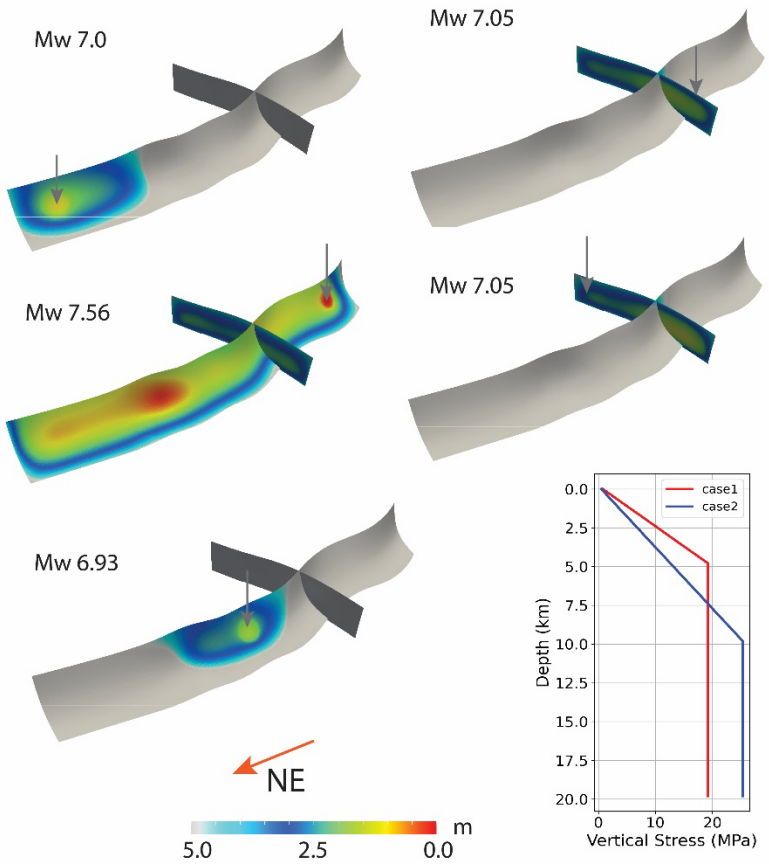

Figure 8 Simulations (model E3~C3 in Table 1) of the case 2 for depth-dependent vertical stress, the lower right sub-figure shows two different depth-dependent stress configurations with critical depth 5 km and 10 km.

6.2 Pattern of rupture in the WMF and LXF fault system

The earthquake scenarios from all simulations in Table 1 can be summarized as six patterns shown in Figure 9a. The 20 cases tested do not cover the entire range of possibilities, and the assigned probabilities remain arbitrary, such as uncertainty of geometry and initial stress are not fully considered. However, the proposed scenarios in this study are fully understandable from the standpoint of the mechanics and, therefore, appear likely. The spatial heterogeneity introduced in this study originates from fault geometry and inverted regional stress, which principally controls the macroscopic patterns. For instance, cascading ruptures tend to jump from oblique fault to strike-slip fault, but the reverse process is more difficult to occur. The ruptures tend to be arrested on the WMF on serval parameter spaces while tend to easily run through the entire LXF (Figure 9a). In addition, the rupture propagating eastward causes greater coseismic displacements than the westward propagations.

A statistical analysis of the moment magnitude, based on the deterministic simulation results, is presented in Figure 9b. We find the earthquake scenarios fall into three groups: those of magnitudes are around 7.5,

7.0 or near 6.6. The first group gathers earthquakes that start on the WMF and could propagate all or most parts of the two faults. The earthquakes with magnitudes around 7.0 usually come from the LXF, or local ruptures on the WMF. The third group gathers earthquakes that start on the WMF but quickly stop near the nucleation patch due to the unfavorable fault orientation given the friction parameters and on-fault stress.

Incorporating all earthquake scenarios to further assess the possible seismic risk in the future, we calculate the maximum surface displacements shown in Figure 10. Static surface deformation plays a crucial role in near-source earthquake hazard analysis. In 2008 Wenchuan Earthquake, the maximum surface displacements are distributed in the two patches underneath Yingxiu and Beichuan towns, leading to the two areas suffering the most intensive shock (Hao et al., 2009; Shen et al., 2009; Tang et al., 2021a). From Figure 10, we find that the two prominent peaks are distributed in the areas of 40 km and 100 km along-strike distance. The Wenchuan town is near the edge of the moderate slip, while the Maoxian town are in the range of the larger slip. Besides, the PGV distributions from the worst scenarios indicate PGV is relatively high when a rupture nucleates at the center or eastern end of WMF. Consequently, Waoxian can suffer a higher seismic risk than Wenchuan in the viewpoint of the source processes .

We also find the value of $\mu_d = 0.12{\sim}0.15$ from all modes are slightly lower than those used in Wenchuan earthquake simulations ($\mu_d = 0.18$) (Zhang et al., 2019; Tang et al.,2021a). If the same friction parameters are used in this study, ruptures will be hard to break in the designed nucleation zone. This is because the steeper dip angle near the surface of the WMF (Figure 4) tends to increase the normal stress, enhancing the fault clamping effect and making it more difficult to slip. Thus, if our model of the WMF with the steeper dip angle is correct, the WMF may cause the lower seismic risk than the BCF with a lower dip for a long-term geological time.

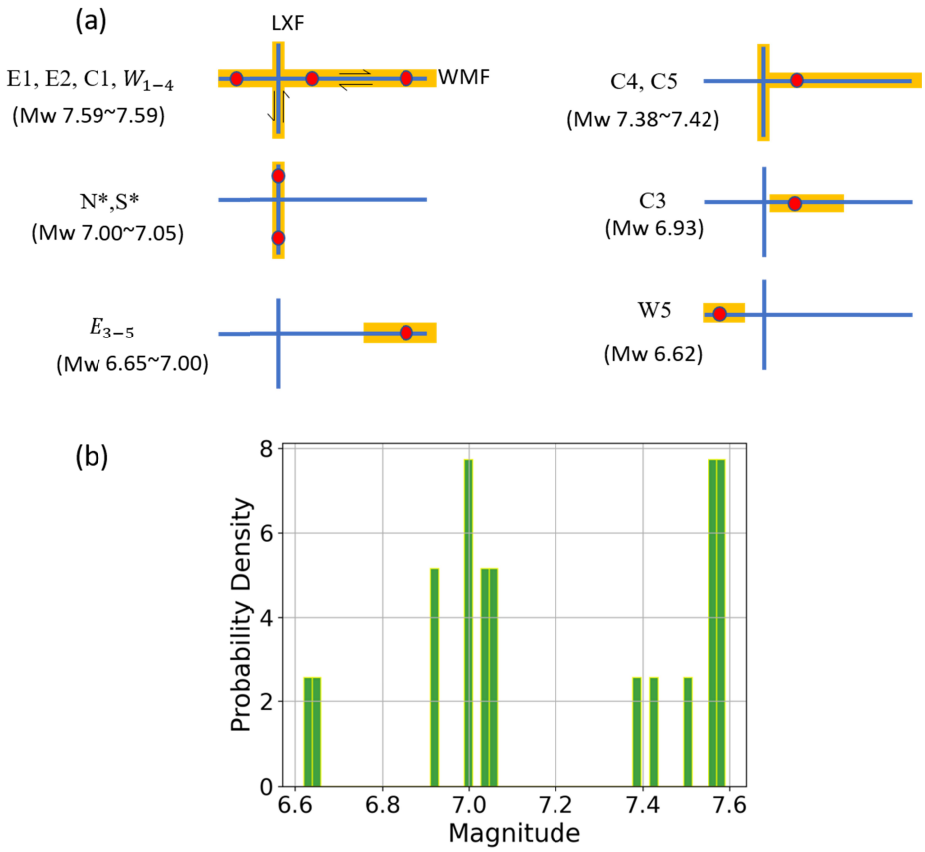

Figure 9 Slip patterns from all models using simple schematic diagrams (a) and histogram of the magnitudes (Mw) obtained in the 20 simulations (b). Yellow highlighting indicates the path of propagating rupture, and solid red circles denote the nucleation sites.

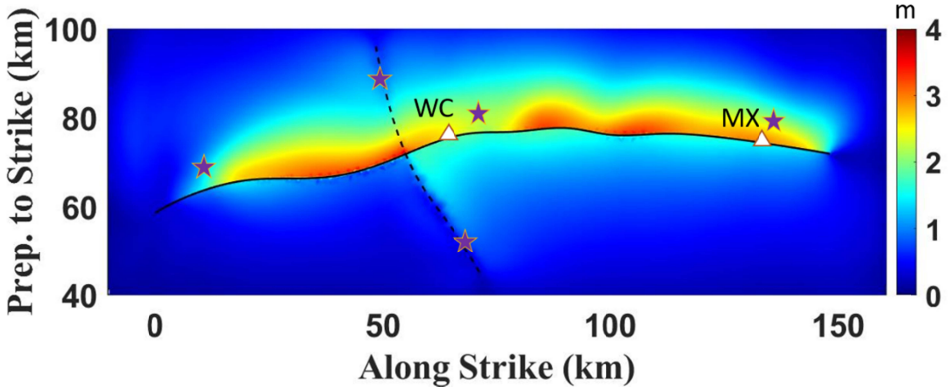

Figure 10 The map for maximum surface displacements from 20 simulations. The white triangles present the two main cities (Wenchuan and Maoxian) and red stars denote the epicenters.

6.3 Explanation for rupture Patterns

We have completed the simulation of the worst earthquake scenarios (model E1~C1), and predicted possible high seismic risk areas. It is noted that there are two interesting scientific issues worthy of further

discussion. First, why do cascading ruptures tend to jump from oblique fault to strike-slip fault, but the reverse process is more difficult? Second, why does the rupture propagating eastward cause greater coseismic displacements than the westward propagation? Although we have mentioned that the rupture directivity can explain the second question, here we hope to further explore the deeper reasons from the perspective of mechanics.

To answer the first question, we calculate the shear stress changes $\Delta\tau$ and normal stress change $\Delta\sigma$ (positive in compression), as well as the Coulomb failure stress change (ΔCFS) on the two faults, under the state when a rupture is approaching the fault intersection (Figure 11). ΔCFS is calculated from $\Delta CFS = \Delta\tau - \mu_s\Delta\sigma$ (Harris,1998), measuring whether the fault tends to be slip (positive) or stable (negative) (Freed, 2005; Parsons et al.,2008; Liu et al.,2018). We found that the rupture nucleating at the east or west end of the WMF approaches the fault intersection can induce obvious positive ΔCFS on the LXF. The main contribution of the increase in ΔCFS comes from $\Delta\tau$ rather than $\Delta\sigma$, although the normal stress change affects a larger area on the LXF. On the other hand, the rupture nucleating at the north or south end of the LXF approaches the fault intersection can induce obvious negative ΔCFS on the WMF. The ΔCFS in the most area near the intersection of the WMF is negative, although there are small-scale positive ΔCFS locally. The ΔCFS is decreased because the effect of shear stress reduction is lower than that of the normal stress increase, or the effect of shear stress reduction is larger than that of normal stress reduction.

It is noted that the fault activity depends on its prestress state besides ΔCFS. However, it is more difficult to observationally determine the absolute prestress level or when in its seismic cycle than the principal stress orientation and the stress ratio. We should keep in mind that the prediction can be more complicated if we consider further stress heterogeneity than those in our modeling. With such a limitation, compared to the WMF, the LXF possibly has higher initial shear stress (Figure S3). This result means that the LXF will be closer to failure than the WMF. As a consequence, together with the evolution of ΔCFS for the four cases, it is reasonable to expect the cascading ruptures jumping from the oblique fault to the strike-slip fault rather than the reverse propagation.

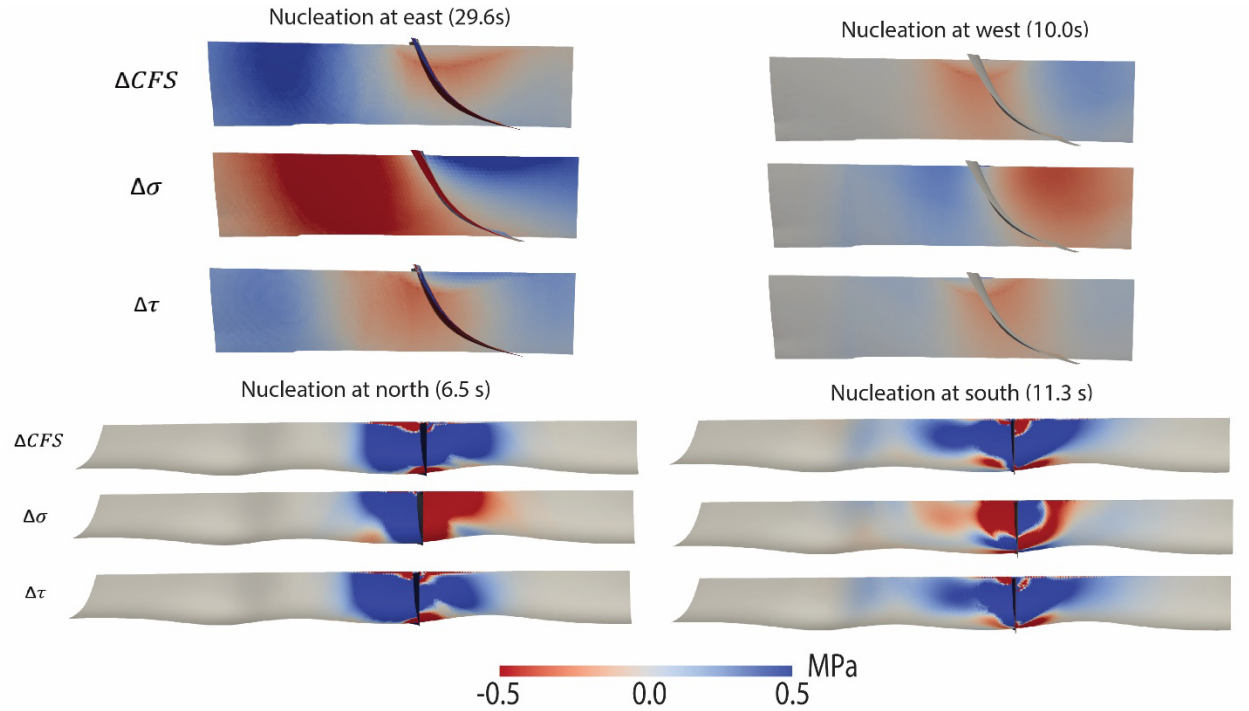

Figure 11 Stress change near the fault intersection when rupture is approaching. Columb failure stress $\Delta CFS(t) = \Delta\tau(t) - \mu_d \Delta\sigma(t)$, where $\Delta\tau$ is shear stress change, $\Delta\sigma$ normal stress change

With regard to the second question, why does the rupture propagating eastward cause greater coseismic slips than the westward propagation. We emphasize that all the conditions in two cases are the same except for the different nucleation position or rupture propagating directivity. The increase of coseismic slips in figure 5b than 5a are distributed almost over the entire fault rather than a local area, which means the stress evolution at a certain point (such as the point shown in Figure 5) on the fault may help reveal the physical mechanism of this phenomenon (Figure 12). The variation of shear stress in two cases are similar in the two cases and the dynamic stress drops are the same, while the normal stress suddenly increases when the rupture propagates from east to west (Figure 12a). The seismic waves generated by rupture superimpose on the edge of rupture front, couple with the hanging wall moving in opposite direction (oblique and dextral slip), forming a local compression. This transient increase of normal stress has suppressed slip rate to reach a large peak value (Figure 12c), resulting in a lower coseismic slip than that of reverse propagating directivity. Our result is consistent with the study of Tang et al (2021b).

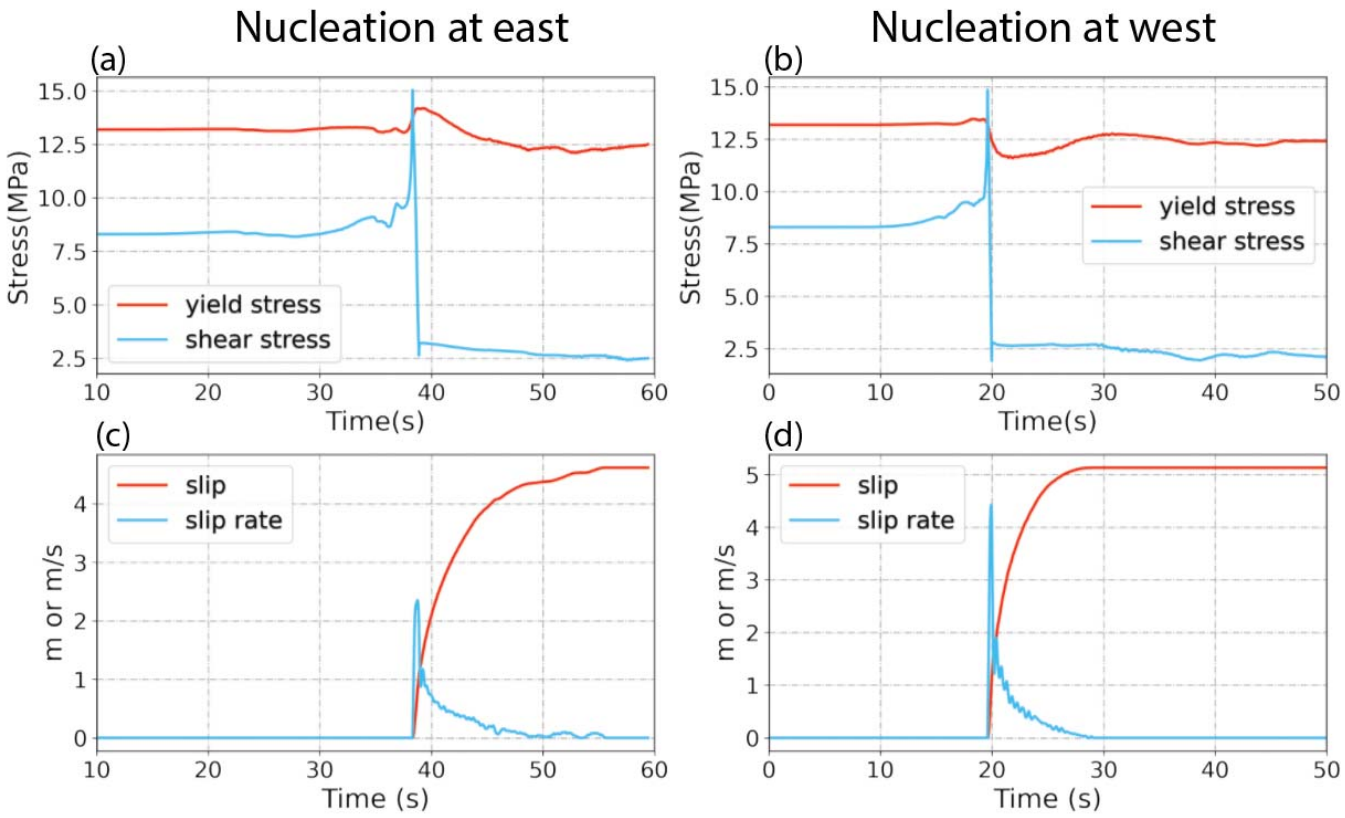

Figure 12 Evolution of stress and slip for the cases with different nucleation positions. The location of fault point is indicated in Figure 5.

7 Conclusion

In this study, we demonstrate an effective technical process, including inversion techniques of the regional tectonic stress and fault geometry, to simulate a dynamic process of active faults, which is helpful in predicting a future earthquake scenario.

We have developed a new algorithm based on the stress state and the Wallace-Bott hypothesis for inversion of fault geometry, and we have obtained non-planar fault surfaces with heterogenous dip angles. In the absence of other geophysical or geological data to constrain fault geometry, this is an effective scheme to obtain relatively accurate faults, with only a small number of long-term slip rate data being used.

Combining deterministic simulations of earthquake dynamics makes it possible to quantify probable rupture scenarios for future earthquakes in the target area, the fault system of the Wenchuan-Maoxian Fault and Lixian Fault. This process is to clarify the mechanical causality of the dynamic system. Numerical simulation results forecast the possible size of the earthquakes occurring on the WMF and LXF in the future while the timing is out of focus. The potential high seismic risk areas are found to be

largely dependent on where the earthquake nucleates. In addition, we have two general conclusions with regard to the system of a reverse oblique fault with a conjugate strike-slip fault. Due to the positive Coulomb Failure Stress change near the fault intersection, the rupture starting on the reverse oblique-slip tends to jump to the strike-slip fault, but the reverse process is difficult because negative Coulomb Failure Stress change dominates near the intersection. Besides, the ground motion will be enhanced if the rupture propagating direction is consistent with the movement direction of the hanging wall because a local compression forms in the counterpart case, suppressing the coseismic slip.

Acknowledgement

Acknowledgement for the data support from China Earthquake Networks Center, National Earthquake Data Center (https://data.earthquake.cn/). Videos in this paper can be download from https://zenodo.org/record/7077841#.YyGRFnZBxD8. This work is supported in part by MEXT, Japan, under its Earthquake and Volcano Hazards Observation and Research Program, and Basic Scientific Research Program from Yangtze Delta Region Institute (U032200109), as well as China Scholarship Council. Oakforest-PACS in University of Tokyo was used for the numerical simulations under the "Joint Usage/Research Center for Interdisciplinary Large-scale Information Infrastructures" and "High Performance Computing Infrastructure" in Japan (Project ID: jh210023-NAH). The authors thank Junjie Ren, So Ozawa and Tawei Chang for providing helpful suggestions.

Reference

Ando, R. (2016). Fast domain partitioning method for dynamic boundary integral equations applicable to non-planar faults dipping in 3-D elastic half-space. Geophysical Journal International, 207(2), 833–847. https://doi.org/10.1093/gji/ggw299

Ando, R., Imanishi, K., Panayotopoulos, Y., & Kobayashi, T. (2017). Dynamic rupture propagation on geometrically complex fault with along-strike variation of fault maturity: Insights from the 2014 northern Nagano earthquake. Earth, Planets and Space, 69(1). https://doi.org/ 10.1186/s40623-017-0715-2

Ando, R., & Kaneko, Y. (2018). Dynamic rupture simulation reproduces spontaneous multifault rupture and arrest during the 2016 Mw 7.9 Kaikoura earthquake. Geophysical Research Letters, 45(23), 12-875.

Anderson, E.M. (1951) The dynamics of faulting and dike formation with application to Britain. Oliver and Boyd, 2nd Edition, Edinburgh, 133147.Bott, M.H.P., 1959. The mechanisms of oblique slip faulting, Geol. Mag., 96, 109–117.

Cai, C., Yu, C., Tao, K., Hu, X., Tian, Y., Zhang, H., ... & Ning, J. (2011). Spatial distribution and focal mechanism solutions of the Wenchuan earthquake series: Results and implications. Earthquake Science, 24(1), 115-125.

621 Chen, Z. H., Burchfiel, B. C., Liu, Y., King, R. W., Royden, L. H., Tang, W., ... & Zhang, X. (2000).
622 Global Positioning System measurements from eastern Tibet and their implications for India/Eurasia
623 intercontinental deformation. Journal of Geophysical Research: Solid Earth, 105(B7), 16215-16227.
624 DENG Wen-Ze, CHEN Jiu-Hui, GUO Biao, LIU Qi-Yuan, LI Shun-Cheng, LI Yu, YIN Xin-Zhong, QI
625 Shao-Hua. Fine velocity structure of the Longmenshan fault zone by double-difference
626 tomography[J]. Chinese Journal of Geophysics, 2014, 57(4): 1101-1110. doi: 10.6038/cjg20140408
627 Douilly, R., Aochi, H., Calais, E., & Freed, A. M. (2015). Three-dimensional dynamic rupture simulations
628 across interacting faults: The Mw7. 0, 2010, Haiti earthquake. Journal of Geophysical Research:
629 Solid Earth, 120(2), 1108-1128.
630 DING, Y. Y., & LI, Z. K. (2009). The discovery of the geophysical field boundary along Wudu-Wenxian-
631 Lixian line and its significance. Geology in China, 6.
632 Feng, G., Jónsson, S., & Klinger, Y. (2017). Which fault segments ruptured in the 2008 Wenchuan
633 earthquake and which did not? New evidence from near-fault 3D surface displacements derived from
634 SAR image offsets. Bulletin of the Seismological Society of America, 107(3), 1185-1200.
635 Farquharson, C. G., & Oldenburg, D. W. (2004). A comparison of automatic techniques for estimating the
636 regularization parameter in non-linear inverse problems. Geophysical Journal International, 156(3),
637 411-425.
638 Hardebeck, J. L., & Michael, A. J. (2006). Damped regional-scale stress inversions: Methodology and
639 examples for southern California and the Coalinga aftershock sequence. Journal of Geophysical
640 Research: Solid Earth, 111(B11).
641 Hubbard, J., Shaw, J. H., & Klinger, Y. (2010). Structural Setting of the 2008 Mw 7.9 Wenchuan, China,
642 EarthquakeStructural Setting of the 2008 Mw 7.9 Wenchuan, China, Earthquake. Bulletin of the
643 Seismological Society of America, 100(5B), 2713-2735.
644 Hu, F., Oglesby, D. D., & Chen, X. (2021). The effect of depth-dependent stress in controlling free-
645 surface-induced supershear rupture on strike-slip faults. Journal of Geophysical Research: Solid
646 Earth, e2020JB021459.
647 Jia, D., Li, Y., Lin, A., Wang, M., Chen, W., Wu, X., ... & Luo, L. (2010). Structural model of 2008 Mw
648 7.9 Wenchuan earthquake in the rejuvenated Longmen Shan thrust belt,
649 China. Tectonophysics, 491(1-4), 174-184.
650 Kanamori, H., & Anderson, D. L. (1975). Theoretical basis of some empirical relations in
651 seismology. Bulletin of the seismological society of America, 65(5), 1073-1095.
652 Li, Y., Jia, D., Shaw, J. H., Hubbard, J., Lin, A., Wang, M., ... & Wu, L. (2010). Structural interpretation
653 of the coseismic faults of the Wenchuan earthquake: Three-dimensional modeling of the Longmen
654 Shan fold-and-thrust belt. Journal of Geophysical Research: Solid Earth, 115(B4).
655 Li, X., Hergert, T., Henk, A., Wang, D., & Zeng, Z. (2019). Subsurface structure and spatial segmentation
656 of the Longmen Shan fault zone at the eastern margin of Tibetan Plateau: Evidence from focal
657 mechanism solutions and stress field inversion. Tectonophysics, 757, 10-23.
658 Liu-Zeng, J., Zhang, Z., Wen, L., Tapponnier, P., Sun, J., Xing, X., ... & Ji, C. (2009). Coseismic ruptures
659 of the 12 May 2008, Ms 8.0 Wenchuan earthquake, Sichuan: East–west crustal shortening on oblique,
660 parallel thrusts along the eastern edge of Tibet. Earth and Planetary Science Letters, 286(3-4), 355-
661 370.
662 Lozos, J. C., & Harris, R. A. (2020). Dynamic rupture simulations of the M6. 4 and M7. 1 July 2019
663 Ridgecrest, California, earthquakes. Geophysical Research Letters, 47(7), e2019GL086020.
664 Lu, R., He, D., John, S., Wu, J. E., Liu, B., & Chen, Y. (2014). Structural model of the central Longmen
665 Shan thrusts using seismic reflection profiles: Implications for the sediments and deformations since
666 the Mesozoic. Tectonophysics, 630, 43-53.

667 Ma, B., Su, G., Hou, Z., & Shu, S. (2005). Late quaternary slip rate in the central part of the Longmen
668 Shan fault zone from terrace deformation along the Minjiang River. Seismology and Geology, 27(2),
669 234–242.
670 Matsumoto, S., Yamashita, Y., Nakamoto, M., Miyazaki, M., Sakai, S., Iio, Y., ... & Asano, Y. (2018).
671 Prestate of stress and fault behavior during the 2016 Kumamoto earthquake (M7. 3). Geophysical
672 Research Letters, 45(2), 637-645.
673 Michael, A. J. (1987). Stress rotation during the Coalinga aftershock sequence. Journal of Geophysical
674 Research: Solid Earth, 92(B8), 7963-7979.
675 Michael, A. J. (1984). Determination of stress from slip data: faults and folds. Journal of Geophysical
676 Research: Solid Earth, 89(B13), 11517-11526.
677 Mikumo, T., Olsen, K. B., Fukuyama, E., & Yagi, Y. (2003). Stress-breakdown time and slip-weakening
678 distance inferred from slip-velocity functions on earthquake faults. Bulletin of the Seismological
679 Society of America, 93(1), 264-282.
680 Marquardt, D. W. (1963). An algorithm for least-squares estimation of nonlinear parameters. Journal of
681 the society for Industrial and Applied Mathematics, 11(2), 431-441.
682 Madden, T. R., and Mackie, R. L., 1989, Three-dimensional magnetotelluric modeling and inversion,
683 Proc. IEEE, 77, 318–333.
684 Mackie, R. L., and Madden, T. R., 1993, Three-dimensional magnetotelluric inversion using conjugate
685 gradients: Geophys. J. Internat., 115, 215–229.
686 McKinley, S., & Levine, M. (1998). Cubic spline interpolation. College of the Redwoods, 45(1), 1049-
687 1060.
688 Xu, X., Wen, X., Yu, G., Chen, G., Klinger, Y., Hubbard, J., & Shaw, J. (2009a). Coseismic reverse-and
689 oblique-slip surface faulting generated by the 2008 Mw 7.9 Wenchuan earthquake,
690 China. Geology, 37(6), 515-518.
691 Oglesby, D. D., Archuleta, R. J., & Nielsen, S. B. (2000). The three-dimensional dynamics of dipping
692 faults. Bulletin of the Seismological Society of America, 90(3), 616-628.
693 Ran, Y. K., Chen, W. S., Xu, X. W., Chen, L. C., Wang, H., Yang, C. C., & Dong, S. P. (2013).
694 Paleoseismic events and recurrence interval along the Beichuan–Yingxiu fault of Longmenshan fault
695 zone, Yingxiu, Sichuan, China. Tectonophysics, 584, 81-90.
696 Ran, Y., Chen, L., Chen, J., Wang, H., Chen, G., Yin, J., ... & Xu, X. (2010). Paleoseismic evidence and
697 repeat time of large earthquakes at three sites along the Longmenshan fault
698 zone. Tectonophysics, 491(1-4), 141-153.
699 Reches, Z. E. (1987). Determination of the tectonic stress tensor from slip along faults that obey the
700 Coulomb yield condition. Tectonics, 6(6), 849-861.
701 Rice, J. R. 1992. Fault stress states, pore pressure distributions, and the weakness of the San Andreas fault.
702 In International geophysics (Vol. 51, pp. 475-503). Academic Press
703 Rice J R. 1993. Spatio-temporal complexity of slip on a fault. Journal of Geophysical Research. 98
704 (B6),9885-9907.
705 Rodi, W., & Mackie, R. L. (2001). Nonlinear conjugate gradients algorithm for 2-D magnetotelluric
706 inversion. Geophysics, 66(1), 174-187.
707 Shen, Z.-K., Sun, J., Zhang, P., Wan, Y., Wang, M., Bürgmann, R., et al. (2009). Slip maxima at fault
708 junctions and rupturing of barriers during the 2008Wenchuan earthquake. Nature Geoscience, 10,
709 718–724.
710 Shearer, P. M., Prieto, G. A., & Hauksson, E. (2006). Comprehensive analysis of earthquake source
711 spectra in southern California. Journal of Geophysical Research: Solid Earth, 111(B6).

712 Soh, I., Chang, C., Lee, J., Hong, T. K., & Park, E. S. (2018). Tectonic stress orientations and magnitudes,
713 and friction of faults, deduced from earthquake focal mechanism inversions over the Korean
714 Peninsula. Geophysical Journal International, 213(2), 1360-1373.
715 Somerville, P. G., Smith, N. F., Graves, R. W., & Abrahamson, N. A. (1997). Modification of empirical
716 strong ground motion attenuation relations to include the amplitude and duration effects of rupture
717 directivity. Seismological research letters, 68(1), 199-222.
718 Tang, R., Zhu, S., & Gan, L. (2021a). Dynamic Rupture Simulations of the 2008 7.9 Wenchuan
719 Earthquake: Implication for Heterogeneous Initial Stress and Complex Multifault Geometry. Journal
720 of Geophysical Research: Solid Earth, 126(12), e2021JB022457.
721 Tang, R., Yuan, J., & Gan, L. (2021b). Free-Surface-Induced Supershear Transition in 3-D Simulations of
722 Spontaneous Dynamic Rupture on Oblique Faults. Geophysical Research Letters, 48(3),
723 e2020GL091621.
724 Tian, T., Zhang, J., Liu, T., Jiang, W., & Zhao, Y. (2017). Morphology, tectonic significance, and
725 relationship to the Wenchuan earthquake of the Xiaoyudong Fault in Western China based on gravity
726 and magnetic data. Journal of Asian Earth Sciences, 138, 672-684.
727 Trugman, D. T., & Shearer, P. M. (2017). Application of an improved spectral decomposition method to
728 examine earthquake source scaling in Southern California. Journal of Geophysical Research: Solid
729 Earth, 122(4), 2890-2910.
730 Ulrich, T., Gabriel, A. A., Ampuero, J. P., & Xu, W. (2019). Dynamic viability of the 2016 Mw 7.8
731 Kaikōura earthquake cascade on weak crustal faults. Nature communications, 10(1), 1-16.
732 Vavryčuk, V. (2014). Iterative joint inversion for stress and fault orientations from focal
733 mechanisms. Geophysical Journal International, 199(1), 69-77.
734 Wu, J., Yao, D., Meng, X., Peng, Z., Su, J., & Long, F. (2017). Spatial-temporal evolutions of early
735 aftershocks following the 2013 Mw 6.6 Lushan earthquake in Sichuan, China. Journal of
736 Geophysical Research: Solid Earth, 122, 2873–2889. https://doi.org/10.1002/2016JB013706
737 Wan, Y., Shen, Z. K., Bürgmann, R., Sun, J., & Wang, M. (2016). Fault geometry and slip distribution of
738 the 2008 Mw 7.9 Wenchuan, China earthquake, inferred from GPS and InSAR
739 measurements. Geophysical Journal International, ggw421.
740 Wang, Z., Wang, J., & Yang, X. (2021). The role of fluids in the 2008 Ms8. 0 Wenchuan
741 earthquake. Journal of Geophysical Research: Solid Earth, 126, e2020JB019959.
742 Wallace, R.E., 1951. Geometry of shearing stress and relation to faulting, J. Geol., 59, 118–130.
743 WU, J. P., HUANG, Y., ZHANG, T. Z., MING, Y. H., & FANG, L. H. (2009). Aftershock distribution of
744 the MS8. 0 Wenchuan earthquake and 3-DP-wave velocity structure in and around source
745 region. Chinese Journal of Geophysics, 52(1), 102-111.
746 Xie Xinsheng, Jiang Wali, Feng Xiying .2011.Discussi on on appearance of surface fractures along the
747 rear-range of Longmen shan mountain during 2008 Ms8.0 Wenchuan earthquake .Acta Seismologica
748 Sinica, 33(1) :62- 81
749 Xu, X., Wen, X., Yu, G., Chen, G., Klinger, Y., Hubbard, J., & Shaw, J. (2009). Coseismic reverse-and
750 oblique-slip surface faulting generated by the 2008 Mw 7.9 Wenchuan earthquake,
751 China. Geology, 37(6), 515-518.
752 Xu, X., Zhang, Z., Hu, F., & Chen, X. (2019). Dynamic Rupture Simulations of the 1920 Ms 8.5 Haiyuan
753 Earthquake in ChinaDynamic Rupture Simulations of the 1920 Ms 8.5 Haiyuan Earthquake in
754 China. Bulletin of the Seismological Society of America, 109(5), 2009-2020.
755 Yang, N., & Zhang, Y. Q. (2010). Tission-track dating for activity of the Longmenshan fault zone and
756 uplifting of the western Sichuan Plateau. Journal of Geomechanics (in Chinese), 16(4), 359-371.

Yao, D., Walter, J. I., Meng, X., Hobbs, T. E., Peng, Z., Newman, A. V., et al. (2017). Detailed spatiotemporal evolution of microseismicity and repeating earthquakes following the 2012 Mw 7.6 Nicoya earthquake. Journal of Geophysical Research: Solid Earth, 122, 524–542. https://doi.org/10.1002/2016JB013632

Yin, X. Z., Chen, J. H., Peng, Z., Meng, X., Liu, Q. Y., Guo, B., & Li, S. C. (2018). Evolution and distribution of the early aftershocks following the 2008 Mw 7.9 Wenchuan earthquake in Sichuan, China. Journal of Geophysical Research: Solid Earth, 123(9), 7775-7790.

Yi, G., Long, F., & Zhang, Z. (2012). Spatial and temporal variation of focal mechanisms for aftershocks of the 2008 MS8. 0 Wenchuan earthquake. Chinese Journal of Geophysics, 55(4), 1213-1227.

Zhao, B., Shi, Y., & Gao, Y. (2011). Relocation of aftershocks of the Wenchuan M S 8.0 earthquake and its implication to seismotectonics. Earthquake Science, 24(1), 107-113.

Zhang, Y., Feng,W., Xu, L., Zhou, C., & Chen, Y. (2009). Spatio-temporal rupture process of the 2008 greatWenchuan earthquake. Science in China Series D-Earth Sciences, 52(2), 145–154.

Zhang, Y., Wang, R., Zschau, J., Chen, Y. T., Parolai, S., & Dahm, T. (2014). Automatic imaging of earthquake rupture processes by iterative deconvolution and stacking of high-rate GPS and strong motion seismograms. Journal of Geophysical Research: Solid Earth, 119(7), 5633-5650.

Zhdanov, M. S. (2002). Geophysical inverse theory and regularization problems (Vol. 36). Elsevier.